PAPER

Check for updates

Solution-processable perylene diimide-based electron transport materials as non-fullerene alternatives for inverted perovskite solar cells†

German Soto Perez,[a] Shyantan Dasgupta,[be] Wiktor Żuraw, [bf]
Rosinda Fuentes Pineda,[c] Konrad Wojciechowski, [bc] Lethy Krishnan Jagadamma,[d]
Ifor Samuel [d] and Neil Robertson [*a]

Perylene diimide derivatives with different functional groups (OR) in the bay position were synthesised (PDI-1, OR = OC_6H_4OMe; PDI-2, OR = $OC_6H_4CH_2CH_2NHBoc$; PDI-3, OR = $OC_6H_4CO_2Me$) and their optoelectronical properties were characterised. The derivatives were applied as alternative electron transport materials (ETMs) to replace the commonly used PCBM in inverted perovskite solar cells (PSCs). Devices with the structure $ITO/PTAA/Cs_{0.04}(MA_{0.17}FA_{0.83})_{0.96}Pb(I_{0.83}Br_{0.17})_3/ETM/Ag$ (ETM = PCBM or PDI-1, -2 or -3) were fabricated through solution processing techniques. A competitive power conversion efficiency (PCE) of 16.8% was obtained for the PDI-3-based device, which was comparable to the PCBM-based device with PCE of 17.3%. It was found that the electronic nature of the functional groups plays an important role in the charge extraction and band alignment of these small molecular semiconductors.

Introduction

Over the last decade, perovskite solar cells (PSCs) have demonstrated their enormous potential in the photovoltaic field with simple and low-cost fabrication and a remarkable increase in power conversion efficiency from 3.8% in 2009 (ref. 1) to the current record of 25.5%.[2] Although the inherent properties of the organic–inorganic halide perovskites make them outstanding photoactive materials, a great contribution to the rapid development of PSCs is due to the research in device architecture, interface engineering and tailoring of charge transport materials.[3–5] Unlike their dye-sensitised solar cell (DSSCs) predecessor, PSCs were found to perform better when the perovskite absorber is sandwiched between solid charge transport materials; commonly, TiO_2 as electron transport material (ETM) and 2,2′,7,7′-tetrakis-(*N,N*-dip-methoxyphenyl-amine)-9,9′-spirobifluorene (spiro-OMeTAD) as hole transport

material (HTL) are used in an $ITO/ETM/perovskite/HTM/Au$ configuration, also known as a regular or n–i–p architecture.[6] In particular, TiO_2 prevailed as ETM due to its suitable conductivity (0.11×10^{-4} S cm^{-1})[7] and favourable conduction band level (-3.9 eV). However, its photocatalytic nature, its ease of surface defect formation and the high temperature processing, requiring $\sim$500 °C, hinders large-scale manufacturing and limits the choice of substrates.

In order to overcome such drawbacks, perovskite-based absorbers have been studied in other device architectures, such as that akin to organic photovoltaics (OPVs), in which the organic semiconducting absorber layer was substituted by $CH_3NH_3PbI_3$ (MAPI) while leaving the PCBM ETM and PEDOT:PSS HTM unmodified, delivering an initial efficiency of 3.9%.[8] A key point of this PSC was the inverted order of the ETM and HTM within the device compared to the regular architecture which gave birth to an inverted PSC (p–i–n) with an ITO/HTM/perovskite/ETM/Ag configuration. The organic nature of the transport materials enabled the use of flexible substrates due to their low temperature processing (<150 °C). The study of these inverted perovskite solar cells (i-PSCs) notably pushed the efficiency to 20.9% (ref. 9) within a few years. However, since most of the initial attention was drawn to device optimisation and interface engineering, the materials inherited from the initial OPV architecture remained, and most studies still rely on fullerene-based organic semiconductors due to their effective performance.

Although fullerenes possess good energy alignment and suitable electron mobility, the lack of other desirable features

aSchool of Chemistry, University of Edinburgh, Kings Buildings, Edinburgh, EH9 3JJ, UK. E-mail: neil.robertson@ed.ac.uk

bSaule Research Institute, Wroclaw PL 54-130, Poland

cSaule Technologies, Wroclaw PL 54-427, Poland

dOrganic Semiconductor Centre, School of Physics and Astronomy, SUPA, University of St Andrews, St Andrews, KY16 9SS, UK

eFaculty of Materials Engineering and Technical Physics, Poznan University of Technology Piotrowo 3, 60-965 Poznan, Poland

fDepartment of Semiconductor Materials Engineering, Wrocław University of Science and Technology, Wybrzeże Wyspiańskiego 27, 50-370 Wrocław, Poland

† Electronic supplementary information (ESI) available. See https://doi.org/10.1039/d2ta01321e

such as thermal and photochemical stability and cost-effective preparation and purification, remain drawbacks for these n-type organic semiconductors. Compared to fullerenes, non-fullerene organic semiconductors have shown better stability, simpler and more straightforward synthetic procedures and enhanced processability, in addition to low-cost production.[10] For instance, polymers have been widely studied due to the tunability of their electronic properties, as well as the modulation of film morphology and tailored compatibility with the other layers in the device, which leads to improvement in efficiency and stability, however, their typical poor electron mobility requires the use of very thin layers (∼5 nm) hindering their large-scale application.[11] Compared to their polymeric counterparts, small molecule semiconductors possess adjustable packing, monodispersity, high synthetic reproducibility and tunable conductivity. Naphthalene diimides are major representatives of this kind of molecule in inverted PSCs; their commercial availability, ease of synthesis and high solubility in several organic solvents, makes them excellent building blocks.[12] Other π-conjugated systems have so far been less explored, such as perylene diimide derivatives, which have recently attracted a lot of attention as n-type organic semiconductors with high electron mobility (∼8×10^{-2} cm^2 V^{-1} s^{-1} for single crystals)[13] and high thermal, chemical and photochemical stability.[14–16] Perylene derivatives have the advantage of tunability of their optoelectronic properties through simple structural modifications, alongside easy and low-cost synthesis and purification with high yields and reproducibility, making them suitable substitutes for expensive and unstable fullerenes.[17,18] Previous studies have shown the potential of PDIs as ETMs through the use of different functional groups attached to alkyl chains in the imide position,[19–22] Click or tap here to enter text.as dimers or assembles of higher dimensionality[23–27] or as

buffer layer or additive either through solution[28,29] or evaporation techniques.[30]

In this study, three highly soluble perylene diimide electron acceptor molecules (Fig. 1a) were designed based on the core contortion approach,[31,32] making them suitable for solution-processing technique while at the same time avoiding the use of long isolating alkyl chains. PDIs with four substituent groups in the bay position have received limited attention in PSCs[33,34] despite the potential advantages in solubility while maintaining suitable pi-interactions. Their synthesis was carried out through the initial reaction of benzylamines in the imide position and further attachment of different functional groups at the bay positions of each molecule (Fig. 1a). Their optoelectronic properties were characterised and performance as ETMs studied in an inverted perovskite solar cell with the layout Glass/ITO/PTAA/Cs$_{0.04}$(MA$_{0.17}$FA$_{0.83}$)$_{0.96}$Pb(I$_{0.83}$Br$_{0.17}$)$_3$/PDI/BCP/Ag to assess them as potential alternatives to the commonly used PCBM.

Experimental section

Synthesis

Compound **1** was used as starting material for the three different PDI derivatives, it was synthesised following the procedure developed by R. K. Dubey *et al.*[35] Compounds **2** and **3** were synthesised from compound **1** by sequential reactions with the corresponding benzylamine following literature procedures.[36,37]

PDI-1. Compound **2** (0.4 g, 0.54 mmol), 4-methoxyphenol (0.34 g, 2.7 mmol) and K$_2$CO$_3$ (0.19 g, 1.35 mmol) were mixed in *N*-methylpyrrolidone (NMP) (8 ml). The reaction was stirred at 120 °C for 68 h under N$_2$. After cooling to room temperature, the mixture was added dropwise to 40 ml of 1 M HCl solution and vigorously stirred for 1 hour at room temperature. The solid was separated by filtration and successively washed with water and methanol. The product was dried under vacuum and purified by chromatographic column with eluent DCM : MeOH [99 : 1] on neutral Al$_2$O$_3$. The final product was obtained as a purple powder (0.273 g, 46.3% yield). (ESI:MS): [M + H]$^+$ calculated for C$_{66}$H$_{47}$O$_{14}$N$_2$: 1091.3021 and [M + Na]$^+$ calculated for C$_{66}$H$_{46}$O$_{14}$N$_2$Na: 1113.2841; found, 1091.2973 and 1113.2862 respectively. Elemental analysis (CHN) calculated for C$_{66}$H$_{46}$N$_2$O$_{14}$: C: 72.65; H: 4.25; N: 2.57. Found: C: 72.61; H: 4.48; N: 2.50.

PDI-2. Compound **3** (0.22 g, 0.3 mmol), N-BOC-tyramine (0.43 g, 1.79 mmol) and K$_2$CO$_3$ (0.25 g, 1.79 mmol) were mixed in NMP (10 ml) and stirred at 110 °C for 20.5 h. After cooling to room temperature, the mixture was poured into a 0.5 M HCl solution and stirred for 5 minutes. Purification was performed through a chromatographic column with DCM : MeOH [95 : 5] eluent. The product was obtained as a dark-red powder (0.285 g, 61.68% yield). (ESI:MS): [M + Na]$^+$ calculated for C$_{92}$H$_{94}$O$_{16}$N$_6$Na: 1561.66185; found, 1561.6595. Elemental analysis (CHN) calculated for C$_{92}$H$_{94}$N$_6$O$_{16}$: C: 71.76; H: 6.15; N: 5.46. Found: C: 71.89; H: 6.29; N: 5.35.

PDI-3. Compound **3** (0.2 g, 0.27 mmol), methyl-4-hydroxybenzoate (0.25 g, 1.63 mmol) and K$_2$CO$_3$ (0.23 mg, 1.63 mmol) were mixed in NMP (3.6 ml) and stirred for 15 h at
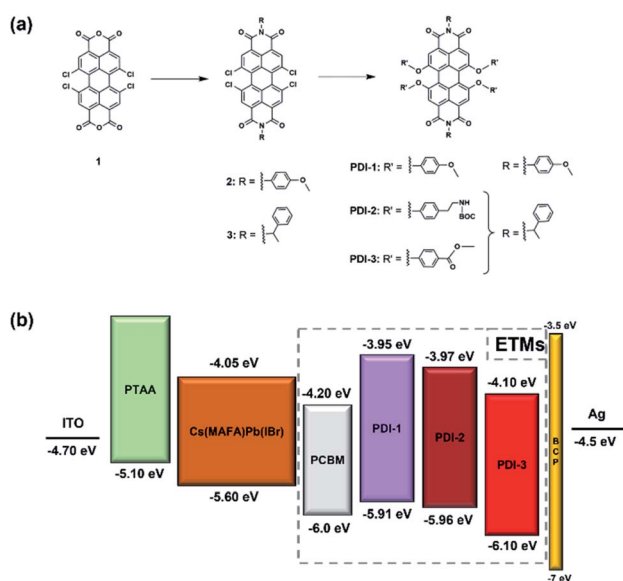

Fig. 1 (a) Molecular structure of the different PDI electron acceptors tested as ETMs, (b) energy band diagram of each material used in the perovskite solar cell.

This journal is © The Royal Society of Chemistry 2022

J. Mater. Chem. A, 2022, **10**, 11046–11053 | **11047**

110 °C under N_2. Once cooled to room temperature, the mixture was added dropwise to a 1 M HCl solution, the precipitate was filtered, dried and purified by chromatographic column with DCM : ethyl acetate [25 : 1] eluent. The pure product was obtained as a red powder (0.25 g, 77.4% yield). (ESI:MS): $[M + Na]^+$ calculated for $C_{72}H_{50}O_{16}N_2Na$: 1221.30526; found, 1221.3056. Elemental analysis (CHN) calculated for $C_{72}H_{50}N_2O_{16}$: C: 72.11; H: 4.20; N: 2.34. Found: C: 72.00; H: 4.30; N: 2.27.

Corresponding NMR spectra and data are shown in Fig. S1.†

Device fabrication

Materials. Unless otherwise stated, all the materials were purchased from Sigma-Aldrich and used as received. Silver pellets were obtained from Kurt Lesker; glass/ITO substrates from Lumtec, and poly-triarylamine (PTAA) from Ossila (product code M0511A5).

Planar heterojunction PSCs were fabricated with the following architecture: ITO/PTAA/$Cs_{0.04}(MA_{0.17}FA_{0.83})_{0.96}Pb(I_{0.83}Br_{0.17})_3$/ETM/Ag (ETM = PCBM or PDI-1, -2 or -3). First, a PTAA solution (1.5 mg ml^{-1} in toluene) was spin coated under ambient conditions at 5000 rpm for 30 s, followed by annealing at 100 °C for 10 min ($\approx$20 nm thick). Subsequently, the samples were transferred into a nitrogen-filled glovebox for the perovskite layer deposition. For the perovskite precursor preparation, stock solutions of PbI_2 and $PbBr_2$ (1.5 M) in dimethylformamide (DMF)/dimethyl sulfoxide (DMSO) mixture [4 : 1 v/v] were prepared. Then, for $FAPbI_3$ and $MAPbBr_3$ solutions, FAI and MABr powders were weighed out into separate vials, followed by addition of PbI_2 (into FAI) and $PbBr_2$ (into MABr) solutions. Both lead solutions were added in excess, to obtain an over stoichiometric lead content (FAI/MABr : PbI_2/$PbBr_2$ equals 1.0 : 1.09). The final perovskite precursor solution was prepared by mixing the solutions of $FAPbI_3$ and $MAPbBr_3$ in a [5 : 1 v/v] ratio. Then, 40 μL of CsI solution (1.5 M solution in DMSO) was added to 1 ml of the mixture. Perovskite layer ($\approx$580 nm thick) was deposited on top of PTAA with a two-step spin-coating procedure, 1500 rpm for 2 s and, 5000 rpm for 34 s. Anhydrous diethyl ether (500 μL) was dispensed on the sample in the last 2 seconds of the spinning sequence. The sample was annealed for 60 min at 100 °C. For the control device, a PCBM solution (20 mg ml^{-1} in chlorobenzene) was spin-coated at 2000 rpm for 30 s and annealed at 60 °C for 10 min. For the devices with PDI-1, -2 and -3 ETM, PDI solutions (20 mg ml^{-1} in chlorobenzene) were spin coated at 4000 rpm for 30 s, The solution-processed ETMs were annealed for 10 min at 60 °C. Finally, 5 nm of BCP buffer layer and 95 nm of Ag electrode were deposited on top of devices by thermal evaporation at $\approx$10^{-6} mbar, through a shadow mask.

Current–voltage measurements. J–V characterization and stabilized power output measurements were performed using a Keithley 2461 source measure unit (SMU) under simulated AM1.5G irradiation (100 mW cm^{-2}) using an AAA-rated solar simulator (Abet Technologies, sun 2000) calibrated against an RR-208-KG5 silicon reference cell (Abet Technologies). The mismatch factor for the studied perovskite solar cells was calculated to be 0.968 using external quantum efficiencies (EQEs) of the reference and test cells, lamp's spectrum, and AM1.5G, and this value was used to correct the intensity of the solar simulator lamp to provide one sun illumination.

Results and discussion

Structural and optoelectronic characterisation

Geometry optimisation of PDI-1 to -3 was carried out through DFT calculations using Gaussian 09 software with the hybrid B3LYP functional and the standard 6-31G(d) basis set for insight into the optoelectronic properties and the core contortion approach that influences the molecular geometry.

Fig. 2 shows that the perylene core in all the PDI derivatives was twisted in the range from 30° to 31° due to the steric effects of the bulky substituents (calculated from the torsion angles (Fig. S2†); the loss of planarity of the molecules led to a higher solubility compared to unsubstituted perylene, which is prone to intermolecular stacking.[38]

All the compounds (measured in solution) exhibited similar optical properties with absorption and emission maxima within the ranges of 560–590 nm and 590–625 nm, respectively (Fig. 3); the shifting between spectra is a result of the electronic interaction between the core and the functional groups attached to it. Compared to the literature values of unsubstituted perylene,[39] PDI-1 and -2 showed a more significant bathochromic shift of $\lambda_{max(abs)}$ due to the electron-donating (ED) nature of the methoxyphenol and the BOC-tyramine groups respectively. In contrast, PDI-3 with the electron-withdrawing (EW) methylhydroxybenzoate substituent showed the shortest absorption and emission wavelengths among the three derivatives.[40]

The linear relation between solutions with different concentrations and their corresponding absorption (Fig. S3†) was used to calculate the molar extinction coefficient of each derivative, the optical data are summarised in Table 1.

The electrochemical properties were measure through square wave voltammetry (SWV) and cyclic voltammetry (CV). The SWV in Fig. 4a shows two reversible reduction peaks, each of which represents a one-electron reduction to the stable radical anion and dianion species, respectively.

The chemical and electrochemical reversibility was confirmed by cyclic voltammetry (Fig. 4b), through the reduction and subsequent oxidation of the product to its original form. In addition, no shift of the current peaks with different
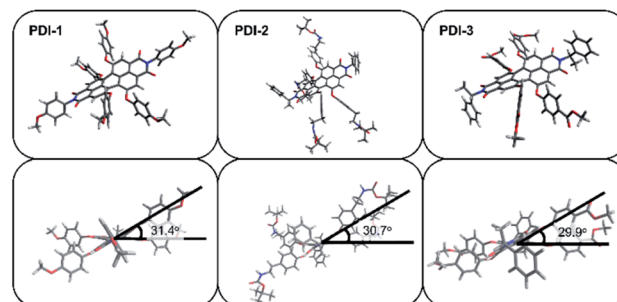

Fig. 2 Calculated geometry of PDI-1 to -3 and their corresponding contortion angle.
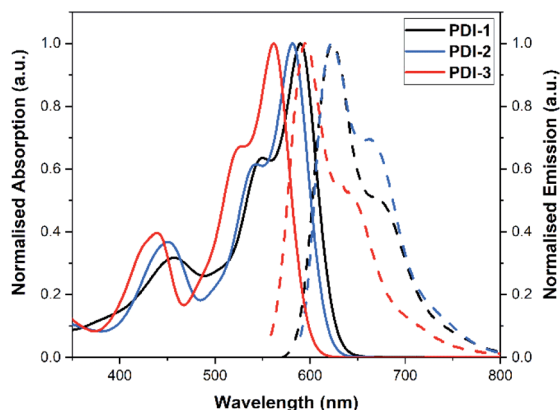
Paper

Fig. 3 Normalised absorption (solid line) and emission (dashed line) spectra of each PDI.

Table 1 Summary of the optical properties of PDI-1 to -3. Literature values of unsubstituted PDI are shown as a ref. 27

Sample	$\lambda_{\mathrm{max(Abs)}}$ [nm]	ε [cm^{-1} M^{-1}]	$\lambda_{\mathrm{max(Em)}}$ [nm]	$E_{\mathrm{gap}}^{\mathrm{opt}\,a}$ [eV]
PDI-1	590	47 200	623	2.04
PDI-2	582	65 200	622	2.05
PDI-3	562	59 300	594	2.14
PDI[27]	525	58 000	553	2.13

^{a} Optical band gap ($E_{\mathrm{gap}}^{\mathrm{opt}}$) was estimated from the intersection of normalised absorption and emission spectra.

scan rates was observed, and a linear relationship between the square root of the scan rate and the current peak was observed.

The electrochemical properties and the calculated levels of highest occupied molecular orbital (HOMO) and lowest unoccupied molecular orbital (LUMO) are summarised in Table 2.

From the data in Table 2, the reduction potentials of the different derivatives are shifted as a result of the electronic nature of the substituents used in each molecule. For instance, PDI-1 has the most negative potentials (due to the high ED nature of the methoxyphenols), followed by PDI-2; whereas PDI-3 has the potentials shifted to more positive values due to the EW nature of the ester group on the substituents. It was also observed that the first reduction potential of each derivative is broadly comparable to the literature value of PCBM ($E_{\mathrm{red}}^{\mathrm{1st}} = -1.16$ V $vs.$ Fc),[41] which suggests that all derivatives could be suitable candidates as PCBM substituents. However, from the calculation of HOMO and LUMO levels using the CV experimental data and the equation:

$$E_{\mathrm{HOMO/LUMO}} = -(E_{\mathrm{ox/red}} + 5.1)\ (\mathrm{eV})\,[42] \tag{1}$$

PDI-3 shows a better band alignment to the conduction band (-4.05 eV (ref. 43)) of the triple cation perovskite used in this work. It is important to keep in mind however, that CV measurements carried out in solution do not account for any solid-state effects on the material within the final device.
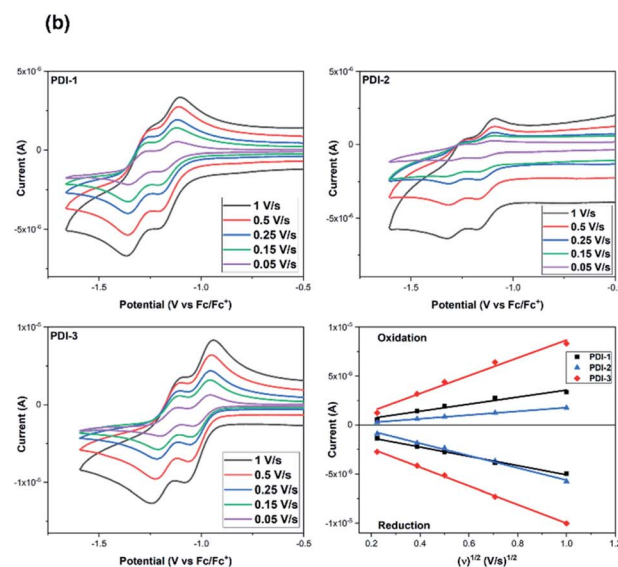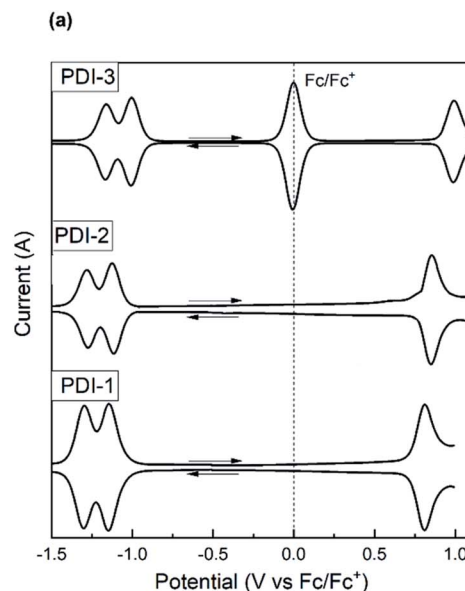

Fig. 4 (a) SWV of PDI-1 to -3, measured at a scan rate of 0.5 V s^{-1}; the arrows indicate the scan direction. (b) CV of PDI-1 to -3 at different scan rates and the linear relation between the square root of the scan rate and the current peak. Both measurements were carried out in a 0.1 M solution of [TBA] [PF$_6$] in DCM at room temperature.

Table 2 Summary of the electrochemical properties of PDI-1, -2, and -3. Corresponding potentials (E) were determined from SWV peaks and are quoted against ferrocene/ferrocenium

Sample	E_{ox} [V]	$E_{\mathrm{red}}^{\mathrm{1st}}$ [V]	$E_{\mathrm{red}}^{\mathrm{2nd}}$ [V]	$E_{\mathrm{gap}}^{\mathrm{CV}}$ [eV]	E_{HOMO} [eV]	E_{LUMO} [eV]
PDI-1	+0.81	−1.15	−1.30	1.96	−5.91	−3.95
PDI-2	+0.86	−1.13	−1.28	1.99	−5.96	−3.97
PDI-3	+1.00	−1.00	−1.15	2.00	−6.10	−4.10

Photophysical characterisation

To investigate the suitability of the derivatives as ETMs, steady-state photoluminescence quenching (PLQ) and time-resolved photoluminescence (TRPL) were measured in glass/perovskite and glass/$Cs_{0.04}(MA_{0.17}FA_{0.83})_{0.96}Pb(I_{0.83}Br_{0.17})_3$/ETM (ETM = PCBM or PDI-1, -2 or -3) devices. The PL spectra in Fig. 5a show an intense emission peak at 760 nm from the perovskite-only device when excited at 405 nm; whereas the devices with the different ETMs (PDI-1 to -3 or PCBM) deposited on top of the perovskite show a significant quenching in emission (PCBM > PDI-3 > PDI-2 > PDI-1). Notably, the emission peak in these devices shows a blue shift of approximately 5 nm, which suggests passivation and reduction of trap density in the ETM/perovskite interface.[44]

TRPL spectra in Fig. 5b shows a similar trend, in which PL lifetime of bare perovskite film (164 ns) decreases upon deposition of PCBM (20 ns), PDI-3 (70 ns), PDI-2 (76 ns) and PDI-1 (79 ns). Collectively, these spectroscopic and electrochemical results indicate the suitability of the PDIs to be tested as ETMs in n–i–p perovskite solar cells.

Additionally, charge mobility studies were carried out, using the space-charge limited current (SCLC) method (Fig. S4†) to assess the electron transport characteristics of the materials. Although it was not possible to observe the trap-free regime, a fit that estimated the trap-filling regime enabled mobilities of the order 10^{-5} cm^2 V^{-1} s^{-1} for PDI-1 and PDI-3 and lower mobility around 10^{-6} cm^2 V^{-1} s^{-1} for PDI-2, consistent with the bulkier substituents of the latter.

Device characterisation

To screen the performance of the ETMs, an initial set of perovskite solar cells with the configuration ITO/PTAA/$Cs_{0.04}(MA_{0.17}FA_{0.83})_{0.96}Pb(I_{0.83}Br_{0.17})_3$/ETM/Ag (ETM = PDI-1 to -3) with a 5 nm buffer layer of BCP in the ETM/Ag interface (Fig. S5†) were fabricated in ITO coated PET substrates and characterised. The PDI solutions were optimised to a concentration of 20 mg ml^{-1} and two different spin coating deposition speeds were tested (2000 (A) and 4000 (B) rpm). Fig. S5c† shows the box plots over eight repeats while Fig. S5b† shows the J–V curves of champion devices with each PDI, and Table 3 summarises the corresponding PV parameters.

Table 3 PV parameters of champion devices tested at different deposition speeds. A and B denotes 2000 and 4000 rpm deposition speed, respectively. Data in parenthesis are the average over 8 devices

| Sample		J_{oc} [mA cm^{-2}]	V_{oc} [V]	FF [%]	PCE [%]
PDI-1	A	7.61 (2.99)	0.84 (0.14)	37.7 (30)	2.60 (0.84)
	B	9.80 (8.51)	0.85 (0.80)	60.2 (50)	5.01 (4.20)
PDI-2	A	0.21 (0.10)	0.69 (0.77)	18.9 (15)	0.03 (0.01)
	B	0.70 (0.15)	0.98 (0.38)	20.6 (18)	0.06 (0.01)
PDI-3	A	16.90 (16.5)	1.01 (0.98)	54.6 (45)	8.70 (8.50)
	B	16.90 (16.1)	1.02 (0.98)	58 (55)	9.80 (7.50)

It was found that PDI-3 was the only derivative suitable to be used as ETM in a full device, delivering the best performance when deposited at 4000 rpm. PDI-1 showed low performance at high-speed deposition whereas low-speed deposition showed an S-type curve, which could be related to a charge accumulation at the PDI-1/perovskite interface due to band offset and non-homogeneous interface.[45] The device with PDI-2 did not show any significant photocurrent output at all.

However, these results are in good agreement with the LUMO energy values calculated previously for the PDI derivatives. In particular, the LUMO level of PDI-3 ($E_{LUMO} = -4.1$ eV) has a suitable energy alignment with the conduction band of the triple cation perovskite ($E_{conduction} = -4.05$ eV)[43] used in the devices, which can also be linked to the PLQ in Fig. 5a, where PDI-3 showed the best quenching among the tested PDIs suggesting better charge extraction from the perovskite photoactive layers compared to the other two ETMs. In contrast, the LUMO values of PDI-1 and -2 (-3.95 and -3.97 eV, respectively) are not as energetically favourable for charge transfer. The apparently poorer (10 times lower) electron mobility of PDI-2 compared to PDI-1 and -3 may also play a role.

Based on the previous results, PDI-3 was used in another set of devices using ITO coated glass substrates and optimising deposition conditions to 5000 rpm (~40 nm film thickness). The results were compared with the well-established solution-processable PCBM ETM (~30 nm film thickness). The J–V plots of champion cells are shown in Fig. 6a, and the PV parameters are summarised in Table 4.

Fig. 6b shows the stabilised power output over time under a bias voltage at maximum power point.[46] A stabilised PCE of 16.5% and 14.5% were observed within 35 s for PCBM and PDI-3 devices, respectively. Fig. 6c shows a high spectral response in the range of 400 to 750 nm for both devices and the integrated current density (derived from the IPCE) is 19.2 and 19.3 mA cm^{-2} for PCBM and PDI-3, respectively. The lower value of the J_{sc} from EQE compared to J_{sc} from J–V plot may account for several reasons such as measuring time, sample degradation or measurement conditions,[47] however, the obtained values are consistent with the trend of J_{sc} values measured in the J–V curves.

The relatively higher J_{sc} of PDI-3 device compared to the PCBM device could be related to a lower rate of recombination in the ETM/perovskite interface, which is in good agreement with the slightly higher value of IPCE for PDI-3 compared to
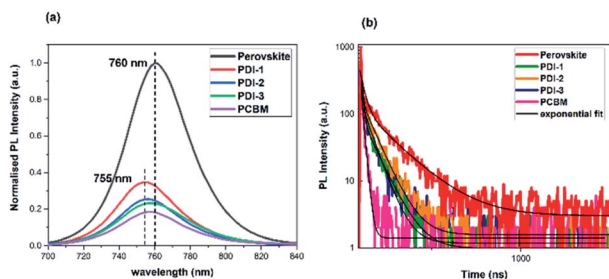
Fig. 5 (a) Steady-state photoluminescence quenching (PLQ). (b) Time-resolved photoluminescence (TRPL) of glass/perovskite and glass/perovskite/ETM devices.
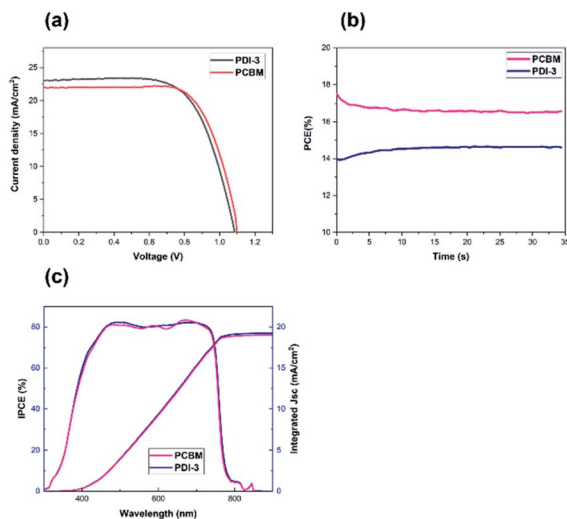
11050 | J. Mater. Chem. A, 2022, **10**, 11046–11053

This journal is © The Royal Society of Chemistry 2022

Fig. 6 (a) J–V curves of champion devices over four repeats. (b) Stabilised power output of PDI-3 and PCBM-based devices. (c) IPCE for PDI-3 and PCBM-based devices and the integrated short circuit current density.

Table 4 PV parameters (reverse scan) of PSCs using PDI-3 or PCBM ETMs. Data in parenthesis are the average over 4 devices

ETM	J_{sc} [mA cm^{-2}]	V_{oc} [V]	FF [%]	PCE [%]
PCBM	22.46 (21.70)	1.09 (1.08)	71.5 (70.7)	17.30 (17)
PDI-3	23.02 (22.80)	1.08 (1.08)	67.5 (64.5)	16.80 (16.10)

PCBM device, as shown in Fig. 6c.[48–50] However, the PCBM device showed a better FF compared to the PDI-3 one, which could be related to a higher mobility of PCBM ($\mu_{PCBM} = 1.22 \times 10^{-3}$ cm^2 V^{-1} s^{-1})[51] compared to that of PDI-3 ($\mu_{PDI-3} = 1.6 \times 10^{-5}$ cm^2 V^{-1} s^{-1}).

Conclusions

In this work, we have designed, synthesised and assessed perylene diimide derivatives as solution-processable ETMs for PSCs. Also, their synthetic versatility and easy tailoring of optoelectronic properties was studied through the attachment of different functional groups (with different electronic nature) to the molecule. Substitution at the bay-positions of the PDI enabled excellent solubility of the molecules while maintaining sufficient charge mobility. Electrochemistry characterisation and LUMO calculations showed that PDI-3 had a better energy alignment with the triple cation perovskite compared to PDI-1 and -2, which indicates that the appropriate control of the electron donating/withdrawing character of functional groups benefits charge extraction through the modulation of electron affinity in the molecule. PLQ and TRPL experiments revealed a comparable charge extraction between commonly used PCBM and PDI-3, indicating that selection of the appropriate side-groups enables performance of PDI-derivatives which is similar to that of PCBM. Accordingly, the champion PDI-3-

based device delivered a PCE of 16.8%, which was comparable to the PCBM-based device with a 17.3% PCE. These results demonstrate that bay-substituted PDIs provide a successful strategy for replacement of PCBM by small-molecule ETM. Further design and tailoring of properties to optimise performance can be achieved through straightforward organic synthetic routes.

Conflicts of interest

There are no conflicts to declare.

Acknowledgements

Notes and references

1 A. Kojima, K. Teshima, Y. Shirai and T. Miyasaka, Organometal Halide Perovskites as Visible-Light Sensitizers for Photovoltaic Cells, *J. Am. Chem. Soc.*, 2009, **131**, 6050–6051.

2 NREL, *Best Research-Cell Efficiency*, **https://www.nrel.gov/pv/cell-efficiency.html**, accessed May 28, 2020.

3 M. A. Green, A. Ho-Baillie and H. J. Snaith, The emergence of perovskite solar cells, *Nat. Photonics*, 2014, **8**, 506–514.

4 M. Grätzel, The light and shade of perovskite solar cells, *Nature Publishing Group*, 2014, **13**, 838–842.

5 J. S. Shaikh, N. S. Shaikh, A. D. Sheikh, S. S. Mali, A. J. Kale, P. Kanjanaboos, C. K. Hong, J. H. Kim and P. S. Patil, Perovskite solar cells: In pursuit of efficiency and stability, *Mater. Des.*, 2017, **136**, 54–80.

6 H.-S. Kim, C.-R. Lee, J.-H. Im, K.-B. Lee, T. Moehl, A. Marchioro, S.-J. Moon, R. Humphry-Baker, J.-H. Yum, J. E. Moser, M. Grätzel and N.-G. Park, Lead Iodide Perovskite Sensitized All-Solid-State Submicron Thin Film Mesoscopic Solar Cell with Efficiency Exceeding 9%, *Sci. Rep.*, 2012, **2**, 591.

7 K. Wojciechowski, M. Saliba, T. Leijtens, A. Abate and H. J. Snaith, Sub-150 °C processed meso-superstructured perovskite solar cells with enhanced efficiency, *Energy Environ. Sci.*, 2014, **7**, 1142–1147.

8 J. Y. Jeng, Y. F. Chiang, M. H. Lee, S. R. Peng, T. F. Guo, P. Chen and T. C. Wen, CH₃NH₃PbI₃ perovskite/fullerene planar-heterojunction hybrid solar cells, *Adv. Mater.*, 2013, **25**, 3727–3732.

9 D. Luo, W. Yang, Z. Wang, A. Sadhanala, Q. Hu, R. Su, R. Shivanna, G. F. Trindade, J. F. Watts, Z. Xu, T. Liu, K. Chen, F. Ye, P. Wu, L. Zhao, J. Wu, Y. Tu, Y. Zhang, X. Yang, W. Zhang, R. H. Friend, Q. Gong, H. J. Snaith and R. Zhu, Enhanced photovoltage for inverted planar heterojunction perovskite solar cells, *Science*, 2018, **360**, 1442–1446.

This journal is © The Royal Society of Chemistry 2022

J. Mater. Chem. A, 2022, **10**, 11046–11053 | **11051**

10 M. Zhang and X. Zhan, Nonfullerene n-Type Organic Semiconductors for Perovskite Solar Cells, *Adv. Energy Mater.*, 2019, **1900860**, 1–12.

11 D. Li, C. Sun, H. Li, H. Shi, X. Shai, Q. Sun, J. Han, Y. Shen, H.-L. Yip, F. Huang and M. Wang, Amino-functionalized conjugated polymer electron transport layers enhance the UV-photostability of planar heterojunction perovskite solar cells, *Chem. Sci.*, 2017, **8**, 4587–4594.

12 Z. Zhang, J. Yuan, Q. Wei and Y. Zou, Small-Molecule Electron Acceptors for Efficient Non-fullerene Organic Solar Cells, *Front. Chem.*, 2018, **6**, 1–22.

13 L.-N. Nguyen, S. Kumar Pradhan, C.-N. Yen, M.-C. Lin, C.-H. Chen, C.-S. Wu, K.-S. Chang-Liao, M.-T. Lin and C.-D. Chen, High performance phototransistors based on single crystalline perylene-tetracarboxylic-dianhydride nanoparticle, *Appl. Phys. Lett.*, 2013, **103**, 183301.

14 H. Langhals, Control of the Interactions in Multichromophores: Novel Concepts. Perylene Bis-imides as Components for Larger Functional Units, *Helv. Chim. Acta*, 2005, **88**, 1309–1343.

15 K. Trofymchuk, A. Reisch, I. Shulov, Y. Mély and A. S. Klymchenko, Tuning the color and photostability of perylene diimides inside polymer nanoparticles: towards biodegradable substitutes of quantum dots, *Nanoscale*, 2014, **6**, 12934–12942.

16 F. Würthner, C. R. Saha-Möller, B. Fimmel, S. Ogi, P. Leowanawat and D. Schmidt, Perylene Bisimide Dye Assemblies as Archetype Functional Supramolecular Materials, *Chem. Rev.*, 2016, **116**, 962–1052.

17 L. Wang, G.-R. Li, Q. Zhao and X.-P. Gao, Non-precious transition metals as counter electrode of perovskite solar cells, *Energy Storage Mater.*, 2017, **7**, 40–47.

18 K. Jiang, F. Wu, H. Yu, Y. Yao, G. Zhang, L. Zhu and H. Yan, A perylene diimide-based electron transport layer enabling efficient inverted perovskite solar cells, *J. Mater. Chem. A*, 2018, **6**, 16868–16873.

19 J. L. Wu, W. K. Huang, Y. C. Chang, B. C. Tsai, Y. C. Hsiao, C. Y. Chang, C. T. Chen and C. T. Chen, Simple mono-halogenated perylene diimides as non-fullerene electron transporting materials in inverted perovskite solar cells with ZnO nanoparticle cathode buffer layers, *J. Mater. Chem. A*, 2017, **5**, 12811–12821.

20 D. Zou, F. Yang, Q. Zhuang, M. Zhu, Y. Chen, G. You, Z. Lin, H. Zhen and Q. Ling, Perylene Diimide-Based Electron-Transporting Material for Perovskite Solar Cells with Undoped Poly(3-hexylthiophene) as Hole-Transporting Material, *ChemSusChem*, 2019, **12**, 1155–1161.

21 J. Huang, Z. Gu, L. Zuo, T. Ye and H. Chen, Morphology control of planar heterojunction perovskite solar cells with fluorinated PDI films as organic electron transport layer, *Sol. Energy*, 2016, **133**, 331–338.

22 H. Zhang, L. Xue, J. Han, Y. Q. Fu, Y. Shen, Z. Zhang, Y. Li and M. Wang, New generation perovskite solar cells with solution-processed amino-substituted perylene diimide derivative as electron-transport layer, *J. Mater. Chem. A*, 2016, **4**, 8724–8733.

23 E. Castro, T. J. Sisto, E. L. Romero, F. Liu, S. R. Peurifoy, J. Wang, X. Zhu, C. Nuckolls and L. Echegoyen, Cove-Edge Nanoribbon Materials for Efficient Inverted Halide Perovskite Solar Cells, *Angew. Chem., Int. Ed.*, 2017, **56**, 14648–14652.

24 S. R. Peurifoy, E. Castro, F. Liu, X. Y. Zhu, F. Ng, S. Jockusch, M. L. Steigerwald, L. Echegoyen, C. Nuckolls and T. J. Sisto, Three-Dimensional Graphene Nanostructures, *J. Am. Chem. Soc.*, 2018, **140**, 9341–9345.

25 R. Wang, K. Jiang, H. Yu, F. Wu, L. Zhu and H. Yan, Efficient inverted perovskite solar cells with truxene-bridged PDI trimers as electron transporting materials, *Mater. Chem. Front.*, 2019, **3**, 2137–2142.

26 F. Wu, Z. Luo, L. Zhu, C. Chen, H. Lu, Z. Chen, J. Tang and C. Yang, Sulfur-annulated perylenediimide as an interfacial material enabling inverted perovskite solar cells with over 20% efficiency and high fill factors exceeding 83%, *J. Mater. Chem. A*, 2019, **7**, 21176–21181.

27 Y. Fan, F. Wu, F. Liu, M. Han, K. Chang, L. Zhu, Q. Li and Z. Li, A perylene diimide dimer-based electron transporting material with an A–D–A structure for efficient inverted perovskite solar cells, *J. Mater. Chem. C*, 2022, **10**, 2544–2550.

28 J. Yang, C. Liu, C. Cai, X. Hu, Z. Huang, X. Duan, X. Meng, Z. Yuan, L. Tan and Y. Chen, High-Performance Perovskite Solar Cells with Excellent Humidity and Thermo-Stability *via* Fluorinated Perylenediimide, *Adv. Energy Mater.*, 2019, **9**, 1900198.

29 J. Min, Z. G. Zhang, Y. Hou, C. O. R. Quiroz, T. Przybilla, C. Bronnbauer, F. Guo, K. Forberich, H. Azimi, T. Ameri, E. Spiecker, Y. Li and C. J. Brabec, Interface engineering of perovskite hybrid solar cells with solution-processed perylene-diimide heterojunctions toward high performance, *Chem. Mater.*, 2015, **27**, 227–234.

30 M. Kaltenbrunner, G. Adam, E. D. Głowacki, M. Drack, R. Schwödiauer, L. Leonat, D. H. Apaydin, H. Groiss, M. C. Scharber, M. S. White, N. S. Sariciftci and S. Bauer, Flexible high power-per-weight perovskite solar cells with chromium oxide-metal contacts for improved stability in air, *Nat. Mater.*, 2015, **14**, 1032–1039.

31 Z. Xie, V. Stepanenko, B. Fimmel and F. Würthner, An organogelator design without solubilizing side chains by backbone contortion of a perylene bisimide pigment, *Mater. Horiz.*, 2014, **1**, 355–359.

32 F. Würthner, C. Thalacker, A. Sautter, W. Schartl, W. Ibach and O. Hollricher, Hierarchical Self-Organization of Perylene Bisimide–Melamine Assemblies to Fluorescent Mesoscopic Superstructures, *Chem.–Eur. J.*, 2000, **6**, 3871–3886.

33 W. Yan, Z. He, J. Jiang, D. Lu, Y. Gong, W. Yang, R. Xia, W. Huang and H. Xin, Highly thermal-stable perylene-bisimide small molecules as efficient electron-transport materials for perovskite solar cells, *J. Mater. Chem. C*, 2020, **8**, 14773–14781.

34 N. Zink-Lorre, E. Font-Sanchis, Á. Sastre-Santos and F. Fernández-Lázaro, Perylenediimides as more than just non-fullerene acceptors: versatile components in organic,

11052 | *J. Mater. Chem. A*, 2022, **10**, 11046–11053

This journal is © The Royal Society of Chemistry 2022

hybrid and perovskite solar cells, *Chem. Commun.*, 2020, **56**, 3824–3838.

35 Z. Xie, V. Stepanenko, B. Fimmel and F. Würthner, An organogelator design without solubilizing side chains by backbone contortion of a perylene bisimide pigment, *Mater. Horiz.*, 2014, **1**, 355–359.

36 T. Kaiser, V. Stepanenko and F. Würthner, Fluorescent J-Aggregates of Core-Substituted Perylene Bisimides: Studies on Structure−Property Relationship, Nucleation−Elongation Mechanism, and Sergeants-and-Soldiers Principle, *J. Am. Chem. Soc.*, 2009, **131**, 6719–6732.

37 C. Yang, Donor/Spacer/Acceptor Block Copolymer Containing Poly(2,7-carbazole) and Perylenetetracarboxydiimide Subunits, *Macromol. Chem. Phys.*, 2010, **211**, 1446–1451.

38 S. Ogi, V. Stepanenko, K. Sugiyasu, M. Takeuchi and F. Würthner, Mechanism of self-assembly process and seeded supramolecular polymerization of perylene bisimide organogelator, *J. Am. Chem. Soc.*, 2015, **137**, 3300–3307.

39 S. H. Oh, B. G. Kim, S. J. Yun, M. Maheswara, K. Kim and J. Y. Do, The synthesis of symmetric and asymmetric perylene derivatives and their optical properties, *Dyes Pigm.*, 2010, **85**, 37–42.

40 C. C. Chao, M. K. Leung, Y. O. Su, K. Y. Chiu, T. H. Lin, S. J. Shieh and S. C. Lin, Photophysical and electrochemical properties of 1,7-diaryl-substituted perylene diimides, *J. Org. Chem.*, 2005, **70**, 4323–4331.

41 C. Yang, S. Cho, A. J. Heeger and F. Wudl, Heteroanalogues of PCBM: N-Bridged Imino-PCBMs for Organic Field-Effect Transistors, *Angew. Chem., Int. Ed.*, 2009, **48**, 1592–1595.

42 C. M. Cardona, W. Li, A. E. Kaifer, D. Stockdale and G. C. Bazan, Electrochemical considerations for determining absolute frontier orbital energy levels of conjugated polymers for solar cell applications, *Adv. Mater.*, 2011, **23**, 2367–2371.

43 I. Gelmetti, N. F. Montcada, A. Pérez-Rodríguez, E. Barrena, C. Ocal, I. García-Benito, A. Molina-Ontoria, N. Martín, A. Vidal-Ferran and E. Palomares, Energy alignment and recombination in perovskite solar cells: Weighted influence on the open circuit voltage, *Energy Environ. Sci.*, 2019, **12**, 1309–1316.

44 D. W. de Quilettes, S. M. Vorpahl, S. D. Stranks, H. Nagaoka, G. E. Eperon, M. E. Ziffer, H. J. Snaith and D. S. Ginger, Impact of microstructure on local carrier lifetime in perovskite solar cells, *Science*, 2015, **348**, 683–686.

45 F. Xu, J. Zhu, R. Cao, S. Ge, W. Wang, H. Xu, R. Xu, Y. Wu, M. Gao, Z. Ma, F. Hong and Z. Jiang, Elucidating the evolution of the current-voltage characteristics of planar organometal halide perovskite solar cells to an S-shape at low temperature, *Sol. Energy Mater. Sol. Cells*, 2016, **157**, 981–988.

46 F. Cai, L. Yang, Y. Yan, J. Zhang, F. Qin, D. Liu, Y.-B. Cheng, Y. Zhou and T. Wang, Eliminated hysteresis and stabilized power output over 20% in planar heterojunction perovskite solar cells by compositional and surface modifications to the low-temperature-processed TiO_2 layer, *J. Mater. Chem. A*, 2017, **5**, 9402–9411.

47 M. Saliba and L. Etgar, Current Density Mismatch in Perovskite Solar Cells, *ACS Energy Lett.*, 2020, **5**, 2886–2888.

48 W. Xu, X. Ma, J. H. Son, S. Y. Jeong, L. Niu, C. Xu, S. Zhang, Z. Zhou, J. Gao, H. Y. Woo, J. Zhang, J. Wang and F. Zhang, Smart Ternary Strategy in Promoting the Performance of Polymer Solar Cells Based on Bulk-Heterojunction or Layer-By-Layer Structure, *Small*, 2022, **18**, 2104215.

49 X. Ma, A. Zeng, J. Gao, Z. Hu, C. Xu, J. H. Son, S. Y. Jeong, C. Zhang, M. Li, K. Wang, H. Yan, Z. Ma, Y. Wang, H. Y. Woo and F. Zhang, Approaching 18% efficiency of ternary organic photovoltaics with wide bandgap polymer donor and well compatible Y6: Y6-1O as acceptor, *Natl. Sci. Rev.*, 2021, **8**, 8.

50 C. Xu, K. Jin, Z. Xiao, Z. Zhao, X. Ma, X. Wang, J. Li, W. Xu, S. Zhang, L. Ding and F. Zhang, Wide Bandgap Polymer with Narrow Photon Harvesting in Visible Light Range Enables Efficient Semitransparent Organic Photovoltaics, *Adv. Funct. Mater.*, 2021, **31**, 52.

51 H. Wang, F. Yang, Y. Xiang, S. Ye, X. Peng, J. Song, J. Qu and W.-Y. Wong, Achieving efficient inverted perovskite solar cells with excellent electron transport and stability by employing a ladder-conjugated perylene diimide dimer, *J. Mater. Chem. A*, 2019, **7**, 24191–24198.

This journal is © The Royal Society of Chemistry 2022

J. Mater. Chem. A, 2022, **10**, 11046–11053 | **11053**